A Three-Dimensional In Vitro Tumor Platform for Modeling Therapeutic Irreversible Electroporation

Christopher B. Arena,[†Δ] Christopher S. Szot,[†Δ] Paulo A. Garcia,[†] Marissa Nichole Rylander,[†] and Rafael V. Davalos[†*]

[†]School of Biomedical Engineering and Sciences (SBES), Virginia Tech-Wake Forest University, Blacksburg, Virginia

ABSTRACT Irreversible electroporation (IRE) is emerging as a powerful tool for tumor ablation that utilizes pulsed electric fields to destabilize the plasma membrane of cancer cells past the point of recovery. The ablated region is dictated primarily by the electric field distribution in the tissue, which forms the basis of current treatment planning algorithms. To generate data for refinement of these algorithms, there is a need to develop a physiologically accurate and reproducible platform on which to study IRE in vitro. Here, IRE was performed on a 3D in vitro tumor model consisting of cancer cells cultured within dense collagen I hydrogels, which have been shown to acquire phenotypes and respond to therapeutic stimuli in a manner analogous to that observed in in vivo pathological systems. Electrical and thermal fluctuations were monitored during treatment, and this information was incorporated into a numerical model for predicting the electric field distribution in the tumors. When correlated with Live/Dead staining of the tumors, an electric field threshold for cell death (500 V/cm) comparable to values reported in vivo was generated. In addition, submillimeter resolution was observed at the boundary between the treated and untreated regions, which is characteristic of in vivo IRE. Overall, these results illustrate the advantages of using 3D cancer cell culture models to improve IRE-treatment planning and facilitate widespread clinical use of the technology.

INTRODUCTION

Irreversible electroporation (IRE) is a nonthermal, focal ablation technique that has shown tremendous promise as an effective cancer therapy (1–7). This procedure uses electrodes to apply a series of short-duration, high-intensity electric pulses through tissue. At the appropriate parameters, the pulses produce irreversible structural changes in the cell membranes within the targeted region, generating a predictable range of cell death with submillimeter resolution (8,9). IRE-based therapy is in the beginning phases of human clinical trials for prostate, kidney, liver, lung, and pancreatic cancer (4–7,10). Because the mechanism of cell death is linked to altered membrane permeability and not thermal processes, IRE spares important extracellular matrix components, such as major blood vessel and nerve architecture (11,12). This enables the treatment of tumors that are normally considered surgically inoperable, due to their close proximity to these sensitive structures (2,3). In addition, IRE is not subject to heat-sink effects from nearby blood flow, and IRE-induced lesions heal rapidly within 2 weeks after treatment (13). The lesion that develops during IRE is visible in real time on multiple imaging platforms (13–16), which is of great benefit to the surgeon, as there can be direct visual confirmation of treatment.

Developing accurate IRE-treatment planning models is essential for the technology to achieve widespread clinical use. Currently, the predictability of IRE outcomes relies upon one's ability to predict the electric field distribution in the tissue and an a priori knowledge of the electric field threshold for cell death given a specific set of pulse parameters (duration, number, repetition rate). This is a complicated task. Altered membrane permeability leads to nonlinear changes in the dielectric tissue properties. In addition, although thermal damage is avoided by properly tuning the pulse parameters, there can still be significant Joule heating within the tissue that influences the dielectric response. Many studies have been performed to investigate the physiological response of various tissue types to IRE pulses without focusing on the engineering aspects of treatment planning (17–20). To the best of our knowledge, the electric field threshold for cell death has only been well documented in vivo for liver tissue (9,21,22), brain tissue (23), and an orthotopic model of mammary tumors in mice (24). Also, studies conducted to elucidate the dynamic relationship between IRE and changes in dielectric properties are limited to experiments on liver (25,26), skin (27), brain (28), kidney (29), and a subcutaneous model of fibrosarcoma in mice (30). Many types of tissue remain unexplored, including a variety of tumors. This can partially be attributed to the cost and difficulty associated with performing in vivo experiments.

A broader literature exists on in vitro cell suspensions (31–33). In this platform, the electric field threshold for cell death can be readily determined using commercially available indicators of membrane integrity or mitochondrial activity. However, there are significant limitations associated with using information derived from this model for treatment planning. Cells in suspension do not provide an accurate representation of their in vivo morphology, and

Submitted July 18, 2012, and accepted for publication September 14, 2012.

[Δ]Christopher B. Arena and Christopher S. Szot contributed equally to this work.

*Correspondence: davalos@vt.edu

Editor: Sean Sun.

0006-3495/12/11/2033/10 $2.00

http://dx.doi.org/10.1016/j.bpj.2012.09.017

the cellular response obtained from these cultures is altered in the absence of cell-cell and cell-matrix interactions. In addition, cells in suspension lack the structural foundation necessary to provide useful spatial information after pulse delivery. To account for spatial information, researchers have proposed using vegetable tissue, such as potato. Potatoes are useful for economically determining field thresholds, because regions subject to IRE are markedly darker (34,35). Also, changes in potato dielectric properties during IRE have been shown to mimic those seen in vivo (34). However, although vegetables are useful for economically investigating trends, it is difficult to draw direct comparisons to tissue with the absence of physiologically responsive cancer cells.

There is a clear need for a system that can be used to model IRE-based cancer therapies and improve treatment planning in a more physiologically relevant manner without requiring the use of animal models. It has been well established in the fields of tissue engineering and cancer biology that cells cultured within a three-dimensional (3D) in vitro environment are capable of acquiring phenotypes and responding to stimuli in a manner analogous to that observed in in vivo biological systems (36–38). We hypothesize that engineering a platform for 3D tumor growth that mimics an in vivo tumor microenvironment will allow the cells to respond to IRE-based therapies in a manner that can be directly related to an in vivo response and therefore have direct clinical impact. Several groups have investigated the phenotypic response of culturing cancer cells in a 3D in vitro environment (39–41). Specifically, our group has developed 3D bioengineered tumors that exhibit phenotypic characteristics representative of in vivo cancer progression (40). This model involves culturing cancer cells within dense collagen I hydrogels, which facilitates proper cell-cell and cell-matrix interactions and encourages the development of a necrotic core, intracellular levels of hypoxia, and angiogenic potential. Therefore, these collagen I hydrogel-based bioengineered tumors can potentially be used for more accurate modeling of IRE-based cancer therapies in an in vitro setting.

In this study, a 3D cancer cell culture model is introduced for improving IRE-treatment planning. Changes in electrical conductivity and temperature were measured for a range of applied voltages. In addition, the role of cell concentration was explored in producing an electrically relevant model of tissue. After treatment, a Live/Dead assay was performed on intact constructs to demonstrate the relationship between the applied voltage and the extent of cell death. Select samples were fixed and processed for hematoxylin and eosin (H&E) staining. All data generated were incorporated into a numerical model. This allowed for the accurate determination of the electric field threshold for cell death (500 V/cm). These results were then compared to experiments using in vitro cell suspensions, which predicted a much higher threshold for cell death (1500 V/cm), illustrating the benefits of 3D cell culture models for IRE-treatment planning.

MATERIALS AND METHODS

Cell culture

Primary dispersed murine pancreatic cancer cells (provided by Dr. Dieter Saur, Technische Universität München, Munich, Germany) were established from pancreatic ductal adenocarcinomas (PDACs) of $Ptf1a^{Cre/+}$; $LSL\text{-}Kras^{G12D/+}$ mice on a C57Bl/6J genetic background. Specifically, primary pancreatic tumors (PPTs) were removed from a mouse (number 8182) and digested in 10 ml Dulbecco's modified Eagle's medium (DMEM) containing 150 U/ml collagenase Type 2 (Worthington, Lakewood, NJ) as described (42). Single PPT-8182 cell suspensions were cultivated in DMEM (supplemented with L-glutamine, ATCC, Manassas, VA) containing 10% fetal bovine serum (Sigma Aldrich, St. Louis, MO) and 1% penicillin/streptomycin (Invitrogen, Carlsbad, CA). These cells have been shown to replicate human pancreatic cancer in terms of histology, metastasis, and genetic alterations (42–44).

Collagen I hydrogel in vitro tumors

Collagen I hydrogel-based in vitro tumors were fabricated as described previously (40). Briefly, Sprague Dawley rat tail tendons were dissolved in 10 mM HCL under agitation overnight, the suspension was centrifuged at 22,500 $\times$ g for 45 min, and the supernatant containing the collagen I was decanted. The concentration of the collagen I solution was calculated using dry-weight measurements, and the solution was sterilized by layering chloroform beneath the collagen I for 24 h. A neutralizing buffer containing 10$\times$ DMEM (Mediatech, Manassas, VA), 1N NaOH, and dH_20 was used to resuspend a pellet of PPT-8182 cells to obtain a final seeding density of 5×10^5 or 50×10^5 cells/ml. The cell suspension was then gently mixed on ice with an appropriate volume of collagen I to achieve a concentration of 8 mg/ml, which provides a matrix stiffness close to measured values for in vivo tumors (45), and pipetted into 10-mm-diameter cylindrical molds. After a 20-min polymerization period at 37°C, the cancer-cell-seeded hydrogels were removed from the molds and cultured in complete media overnight before IRE pulse delivery. It is important to note that the 5×10^6 cells/ml seeding density was used in a majority of the experiments, because this was found to adequately maintain cell viability throughout the construct over a 24-h period. The seeding density of 50×10^6 cells/ml was used to investigate whether a higher concentration of cells could modulate the electrical properties of the in vitro tumors. Control hydrogels were also fabricated using the neutralizing buffer alone without cells as a comparison to elucidate any effects due to electroporation.

IRE pulse delivery for in vitro tumors

In vitro tumors were temporarily removed from media and placed in six-well plates for IRE pulse delivery. Pulses were applied through custom electrodes (1.3 mm Ø) fabricated from stainless steel hollow dispensing needles (Howard Electronic Instruments, El Dorado, KS) using the ECM 830 electroporation system (BTX-Harvard Apparatus, Holliston, MA) (Fig. 1 *a*). The pulse duration (100 μs), number (80 pulses), and repetition rate (1 pulse/s) were held constant and chosen based on established protocols (8,46). In the 5×10^6 cells/ml seeded in vitro tumors, the applied voltage was varied (0 V, 150 V, 300 V, 450 V, and 600 V) to generate voltage/distance ratios of 0–1800 V/cm across the 3.35-mm electrode spacing (center to center). In the no-cells control and 50×10^6 cells/ml seeded in vitro tumors, the applied voltage was held constant at 300 V. Before the full IRE protocol, a prepulse was delivered at 30 V to determine the baseline electrical conductivity of the in vitro tumors. A port located 2.3 mm below the center point between the electrodes was included in

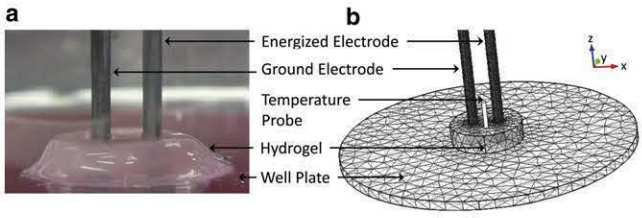

FIGURE 1 (*a*) Experimental setup for IRE pulse delivery in collagen I hydrogel-based in vitro tumors in which PDAC cells are embedded. (*b*) Geometry and mesh used in the finite element model for simulating the electrical and thermal response of the in vitro tumors to IRE.

the electrode design to monitor temperature in real time during treatment with a fiber optic probe (Luxtron m3300, LumaSense Technologies, Santa Clara, CA). In addition, current (TCP305 and TCPA300, Tektronix, Beaverton, OR) and voltage (P5200, Tektronix) were recorded noninvasively during treatment. The generated temperature, current, and voltage data were used to validate the numerical model for predicting the electric field threshold for IRE (see Results, Numerical model validation). Further, to eliminate the influence of the temperature probe on the electrical measurements, samples used for monitoring temperature were separate from those used for performing the viability analysis. After each treatment, the tumor diameter and thickness were measured with calipers for use in determining electrical properties. Each parameter combination was tested a minimum of three times ($n = 3$).

Viability analysis for in vitro tumors

After IRE pulse delivery, the in vitro tumors were incubated in complete media for 2 h before conducting a Live/Dead assay to allow any cells experiencing reversible electroporation to fully recover. Calcein acetomethoxy (AM) (4 μM; $\lambda_{em} = 515$ nm; Invitrogen) was added to the media 30 min before analysis, and propidium iodide (1.5 mM; $\lambda_{em} = 617$ nm; Invitrogen) was added to the media 5 min before analysis. Calcein AM stains live cells, as it can be transported across the cell membrane and fluoresces when intracellular esterases remove the attached AM group. Propidium iodide (PI) fluorescently labels dead cells, as it only enters compromised cell membranes and binds to nucleic acids. A Leica DMI 6000 fluorescent microscope (Leica Microsystems, Buffalo Grove, IL) was used to tile a set of images and reconstruct the entire surface of the IRE-treated in vitro tumors. A Zeiss LSM 510 laser scanning confocal microscope (Carl Zeiss, Thornwood, NY) was used to analyze the live-dead cell interface and reconstruct a Z-stack. Viability imaging was performed on complete, nonsectioned in vitro tumors.

In addition, cytoskeletal disruption within the IRE-treated regions was investigated. The tumors were stained with rhodamine phalloidin (Invitrogen), a high-affinity probe for F-actin, and NucBlue fixed cell stain (Invitrogen) to visualize nuclei. The samples were then routinely fixed in 10% formalin, paraffin-embedded, and sectioned at 5 μm for histological analysis. An H&E stain was performed to further analyze cell death within the IRE-treated regions.

Analysis of IRE on cell suspensions

The details of the methods associated with IRE pulse delivery and viability analysis for cell suspensions can be found in the Supporting Material.

Numerical modeling

Description of the model geometry and mesh

Finite element analysis software (COMSOL Multiphysics 4.2a, Stockholm, Sweden) was used to solve for the electric field and temperature distributions within the in vitro tumor during IRE therapy. A 3D geometry was constructed with dimensions equivalent to those in the experimental setup (Fig. 1 *b*). Each treatment was performed in a single well of a polystyrene six-well plate with a thickness of 1.2 mm and radius of 1.9 cm. The stainless steel electrodes had a length of 5.5 cm through which heat could dissipate. A finer mesh was used that consisted of 67,557 tetrahedral elements. This resulted in a <0.02% difference in temperature calculations at the site of the fiber optic probe upon successive refinements.

Determination of baseline electrical properties

To solve for the baseline electrical conductivity of the in vitro tumors, a three-variable parametric study was performed on the tumor radius (4.5, 4.75, and 5 mm), thickness (2, 2.5, and 3 mm), and conductivity (0.25, 0.5, 0.75, 1.0, 1.25 S/m) using the numerical model. Based on the pulse characteristics associated with IRE and the subdomain dielectric (Table 1) and geometry properties, propagation effects and transients were assumed to be negligible, and the quasistatic approximation was implemented (47,48). This allows for definition of the electric field magnitude as $E = -\nabla\phi$, where ϕ is the electric potential. Therefore, the spatial distribution of electric potential can be expressed as

$$0 = -\nabla \cdot (\sigma_0 E), \tag{1}$$

where σ_0 is the baseline electrical conductivity. Equation 1 was used to solve for the total current flowing in the in vitro tumor when a constant 30 V prepulse was applied to the energized electrode, with the other electrode set as ground. Specifically, the magnitude of the current density (J) was integrated over a cut plane dividing the geometry in half between the electrodes. All outer boundaries, excluding the electrodes, were assumed to be electrically insulating ($-n \cdot J = 0$), and the initial voltage (V_0) within each subdomain was 0 V.

The resulting data relating current (I) to each parameter combination were imported into Mathematica 8.0 (Wolfram, Champaign, IL). A regression analysis was performed to determine the baseline electrical conductivity using the measured current from the prepulse routine along with the corresponding tumor dimensions.

For comparison to the experimentally determined values for in vitro tumor baseline electrical conductivity, a theoretical calculation was performed using effective medium theory (EMT) (49). Specifically, Maxwell's equation for a dilute suspension was solved for the effective conductivity, σ:

$$\frac{\sigma_e - \sigma}{2\sigma_e + \sigma} = f\frac{\sigma_e - \sigma_p}{2\sigma_e + \sigma_p}, \tag{2}$$

where σ_e is the extracellular medium conductivity (1.2 S/m), σ_p is the homogeneous particle conductivity (0.2×10^{-4} S/m for an equivalent cell (49)), and f is the volume fraction of particles dispersed in the medium. Equation 2 is valid for predicting the low-frequency effective conductivity of a cell suspension for volume fractions up to 0.8 (50). This allowed for extrapolations of tumor baseline conductivity at cell concentrations higher than those tested experimentally to estimate what cell concentration would be required to be electrically similar to tissue.

TABLE 1 Physical properties used in numerical simulations

Parameter	Tumor	Electrode†	Plate‡
k (W m^{-1} K^{-1})	0.6	14	0.14
c (J kg^{-1} K^{-1})	4181.8	477	1300
ρ (kg m^{-3})	997.8	7900	1050
σ_0 (S m^{-1})	1.2	2.22×10^6	1×10^{-16}

†Electrode numerical data are taken from Al Sakere et al. (46).
‡Plate numerical data are taken from Chiu and Fair (67).

Determination of transient current and temperature development

The temperature distribution (T) within the in vitro tumor was obtained by transiently solving a modified heat conduction equation with inclusion of the Joule heating-source term ($J \cdot E = \sigma|E|^2$):

$$\rho c \frac{\partial T}{\partial t} = \nabla \cdot (k \nabla T) + \frac{\tau(\sigma|E|^2)}{P}, \quad (3)$$

where τ is the pulse duration, P is the period of the pulses, k is the thermal conductivity, c is the specific heat at constant pressure, and ρ is the density (Table 1). Due to the fact that the collagen-I-hydrogel-based tumors have a water content of >98%, the thermal properties of the tumor were chosen to be the same as those of water. The tumor baseline electrical conductivity (1.2 S/m) was determined experimentally from the average of the no-cells and 5×10^6-cells/ml trials (Table 2), as there was no statistical difference between those two groups (see Results, Determination of baseline electrical properties). In addition, the tumor radius (4.705 mm) and thickness (2.45 mm) were also selected by averaging the measurements from the same groups. Equation 1 was modified to include a temperature dependence on electrical conductivity:

$$0 = -\nabla \cdot (\sigma(T)E), \quad (4)$$

where

$$\sigma(T) = \sigma_0(1 + \alpha(T - T_0)) \quad (5)$$

and α is the coefficient that describes how the conductivity varies with temperature. This parameter was estimated to be 2%/°C by optimizing the measured change in temperature and current throughout treatment to match the theoretical changes. The optimization was performed by running a parametric study on α at 0.5%/K increments. A value of 2%/°C is similar to values observed in biological tissue (51).

At each time step, the conductivity and electric field are determined and updated in the Joule heating term. As opposed to simulating individual pulses, a duty cycle approach was employed to calculate the temperature increase resulting from various IRE protocols. A constant voltage (150, 300, 450, and 600 V) was applied to the energized electrode, with the other electrode set as ground. The Joule heating term was scaled by the duty cycle ($\tau/P = 100 \times 10^{-6}$) to ensure that equal amounts of energy were deposited into the tissue by the onset of each pulse. This approach has been validated in our previous work (29,52) as providing an accurate prediction of the temperature distribution with a fraction of the computational requirements necessary to resolve microsecond-order pulses within a treatment lasting several seconds.

All outer boundaries, excluding the outer vertical edge of the well plate, were treated as convective cooling ($-n \cdot (-k\nabla T) = h(T_{ext} - T)$) with an exterior temperature of 22°C and a heat-transfer coefficient of 25 (W m^{-2} K^{-1}). The vertical edge of the well plate was treated as thermally insulating ($-n \cdot (-k\nabla T) = 0$), and the initial temperature (T_0) within each subdomain was the same as the exterior temperature. Intermediate time stepping was used to ensure that at least one time step was taken each second.

TABLE 2 Baseline electrical conductivity from prepulse measurements and EMT theory

Concentration (cells ml^{-1})	Experimental σ_0 (S m^{-1})	Theoretical σ_0 (S m^{-1})
0 ($n = 6$)	1.18 ± 0.09	1.2
5×10^6 ($n = 15$)	1.24 ± 0.11	1.2
50×10^6 ($n = 6$)	1.08 ± 0.08	1.1

Determination of electric field threshold for cell death

After the in vitro tumor viability analysis, the area, height, and width of the treated region were measured using Image J (National Institutes of Health, Bethesda MD) for three samples of each parameter combination and averaged. All measurements were made on the surface of the tumors. The width measurements were taken in the x-direction and the height measurements were taken in the y-direction. The electric-field threshold for cell death was determined in three ways, using the area, height, and width measurements (Table 3). For determining the threshold from the area measurement, the electric field on the top surface of the tumors was integrated at the end of the treatment ($t = 80$ s) for values greater than the threshold value. The threshold value was varied until the area calculation best matched the measured values within 1 V/cm (excluding the area of the electrodes). For determining the threshold from the height and width measurements, the value of the electric field at a point on the surface corresponding to the measurements was taken at the end of treatment.

RESULTS

Physiological response to IRE pulse delivery within in vitro tumors

When the 30 V prepulse was delivered to determine the baseline electrical conductivity of the in vitro tumors, no cell death was observed as a result of the treatment (Fig. 2 *a*). At this low voltage/distance ratio (90 V/cm taken from the center-to-center electrode spacing), any electroporation that may have occurred was reversible (21). Minimal cell death was observed where the electrodes punctured the surface of the tumors. When the electric field strength was increased to 150 V, cell death was observed on the medial side of both electrodes, but the treated regions did not expand far enough to completely connect (Fig. 2 *b*). Rather, a transition zone of both live and dead cells was observed at the center of the two electrodes. At the higher electric-field strengths (300 V and 450 V), the treated region was amplified with increasing electric-field strength, expanding in both the x- and y-directions (Fig. 2, *c* and *d*). The nonspecific regions of cell death present around the periphery of the tumors were a result of handling the samples with tweezers.

A sharp interface between live and dead cells was observed at the threshold boundary for cell death with submillimeter resolution (Fig. 3 *a*). The specificity of these treatments was similar to what has been achieved during in vivo IRE pulse delivery (8,9). Confocal microscopy was used to show that the IRE-induced cell death was uniform in the z-direction (Fig. 3 *b*), demonstrating that the in vitro tumors can provide spatial information in both the xy and z planes. In addition, the 3D reconstruction highlighted the transition zone at the live/dead cell interface where there were clear contrasting gradients of live and dead cells that converged at the threshold boundary for cell death.

Histology was used to further assess the IRE-induced cell death in the in vitro tumors. Again, a sharp interface between live and dead cells was evident from an H&E stain (Fig. 4 *a*). The PPT-8182 cells within the untreated regions

TABLE 3 Treatment dimensions and electric field threshold for cell death

Voltage (V)	Conc. (cells ml^{-1})	Area (mm^2)	Height (mm)	Width (mm)	E_T (Area, Height, and Width) (V cm^{-1})
300 ($n = 3$)	5×10^6	16.28 ± 2.73	4.02 ± 0.40	4.91 ± 0.34	491, 501, 500
450 ($n = 3$)	5×10^6	25.80 ± 1.48	5.83 ± 0.40	5.58 ± 0.13	498, 502, 470

Conc., concentration.

appeared normal with healthy nuclei and complete cytoplasms, signifying that they were not affected by the IRE pulse delivery (Fig. 4 *c*). Conversely, the cells within the IRE-treated regions were completely destroyed except for their remaining nuclei, which appeared abnormal and no longer contained nucleoli (Fig. 4 *b*). The absence of cytoplasmic material indicated that the IRE pulses had irreversibly compromised the cell membranes, leaving clear voids in the collagen hydrogel where the cells had been.

An F-actin stain was performed to determine the effect of the IRE pulses on the actin cytoskeleton of PPT-8182 cells cultured within the in vitro tumors (Fig. 4, *d* and *e*). PPT-8182 cells within the untreated regions had spherical morphologies with high concentrations of actin present around the periphery of the cells (Fig. 4 *e*). Since the tumors were only cultured overnight before IRE pulse delivery, the cells did not proliferate into large clusters or develop invasive processes, as observed previously (40). The cytoskeleton of cells within the IRE-treated regions seems to be permanently disrupted, appearing speckled and faded (Fig. 4 *d*). This suggests that the IRE pulses led to degradation of the actin filaments, which differs from reversible electroporation, where actin filaments have been shown to reassemble 1 h after electroporation (53). The presence of a disrupted cytoskeleton within the IRE-treated cells revealed that some cytoplasmic material was still present after IRE pulse delivery. Over time, this remaining cytoplasm was either fully degraded or washed away during histology preparation (Fig. 4 *b*). In treatment groups where the Live/Dead stain was not performed until 24 h after IRE treatment, there were no visible PI-stained dead cells within the treated regions, indicating that the nuclei had also been fully degraded or washed away (data not shown).

Determination of baseline electrical properties

The baseline electrical conductivity of the in vitro tumors is given in Table 2. A one-way ANOVA was used to investigate the effect of cell concentration on the rank of baseline conductivity. In the event of a significant main effect, pairwise comparisons were completed using Tukey's honestly significant difference (HSD). All statistical analysis were conducted using JMP 9 (SAS Institute, Cary, NC) with a significance level of $p \leq 0.05$. Results indicate that a cell concentration of 50×10^6 cells/ml is high enough to produce a detectable decrease of ~0.1 S/m in baseline conductivity when compared to the 5×10^6 cells/ml group. Further, there is no significant difference in baseline conductivity between the no-cells and 5×10^6 cells/ml groups. These

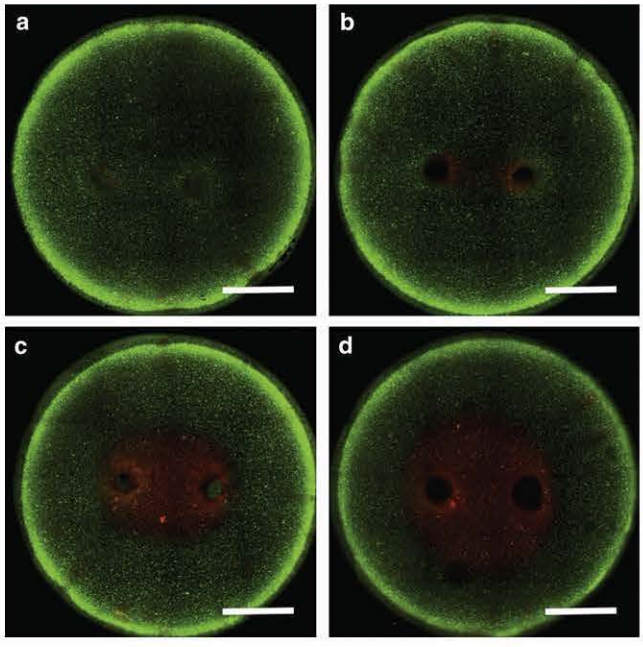

FIGURE 2 A live/dead assay for assessment of cell death after IRE pulse delivery of 30 V (*a*), 150 V (*b*), 300 V (*c*), and 450 V (*d*). Live cells were stained green using Calcein AM and dead cells were stained red using propidium iodide. Images were tiled to reconstruct the entire surface of the IRE-treated in vitro tumors. The bright rings encircling the hydrogels are a consequence of out-of-plane fluorescence at the rounded edges. Scale bars, 2.5 mm.

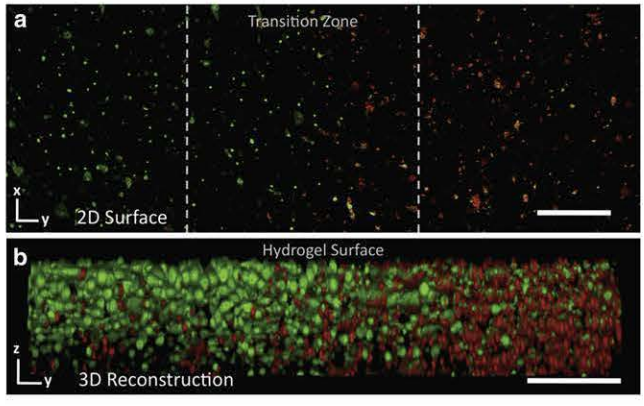

FIGURE 3 (*a*) A sharp interface between live (*green*; *left*) and dead (*red*; *right*) cells at the threshold boundary for cell death with submillimeter resolution. (*b*) 3D reconstruction at this interface highlights the transition zone between live and dead cells and demonstrates that IRE-induced cell death was uniform throughout the in vitro tumors. The dotted lines in (*a*) define the representative region from which the image in (*b*) was taken. Scale bars, 400 μm (*a*) and 200 μm (*b*).

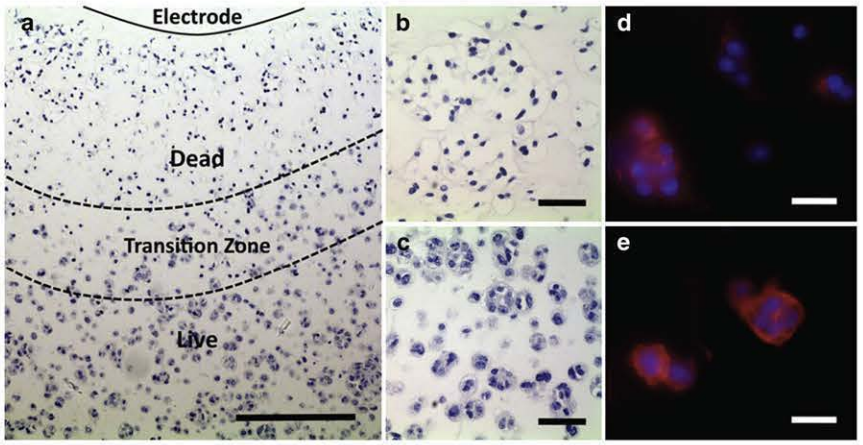

FIGURE 4 (*a*) An H&E stain for further assessment of cell viability after IRE pulse delivery of 450 V through in vitro tumors seeded with 50×10^6 cells/ml. (*b* and *c*) Cells located within the IRE-treated regions appeared to be devoid of most cytoplasmic material (*b*), whereas cells located within the untreated regions appeared normal, with intact cell membranes (*c*). (*d* and *e*) Dotted lines in (*a*) define the transition zone at the live/dead cell interface. An F-actin stain (*red*) was used to determine the effect of IRE-pulse delivery on the cytoskeleton of PPT-8182 cells cultured within the IRE-treated (*d*) and untreated (*e*) regions of the in vitro tumors. The actin cytoskeleton within the IRE-treated cells appears permanently disrupted. Nuclei were stained with DAPI (*blue*). Scale bars, 250 μm (*a*), 50 μm (*b* and *c*), and 25 μm (*d* and *e*).

results agree well with the theoretical calculations based on EMT. Specifically, a cell concentration on the order of 48×10^6 cells/ml is required to reduce the baseline conductivity by 0.1 S/m. This corresponds to a volume fraction of cells of ~0.06.

Numerical model validation

The numerical model was validated through comparisons to experimentally measured changes in current and temperature between the first and last pulse of treatment (Fig. 5). The predicted change in current delivered through the in vitro tumors was accurate around 1 standard deviation at all voltages tested (Fig. 5 *a*). As the applied voltage increased, the change in current during treatment also increased. This change is nonlinear due to the inclusion of a temperature-dependent conductivity. The predicted change in temperature at the location of the fiber optic temperature probe was accurate within a single standard deviation at all voltages tested (Fig. 5 *b*). The temperature change during treatment also increased nonlinearly with the applied voltage. The inclusion of the actual metal electrodes and polystyrene plate was required to dissipate the heat and match experimental temperatures using a reasonable heat-transfer coefficient for free convection with air of 25 W m^{-2} K^{-1} (54).

Determination of transient current and temperature development

Representative surface plots of the predicted electric field, temperature, and electrical conductivity distributions for an applied voltage of 300 V are shown in Fig. 6. The maximum temperature at the end of treatment occurred at the center of the domain. For all simulated voltages, the maximum temperature was calculated to be 23°C, 27°C, 35°C, and 51°C for applied voltages of 150 V, 300 V, 450 V, and 600 V, respectively, with the baseline set at 22°C. Experimentally, an applied voltage of 600 V resulted in the formation of a void at the center of the in vitro tumors, presumably due to collagen denaturation (data not shown) (55). By comparing the dimensions of the void with the temperature distribution, it was conservatively estimated that temperatures >45°C should be avoided in future experiments on this in vitro platform.

Due to the inclusion of a temperature-dependent electrical conductivity, the maximum conductivity at the end of treatment also occurred at the center of the domain. For all simulated voltages, the maximum conductivity was calculated to be 1.2 S/m, 1.3 S/m, 1.5 S/m, and 1.9 S/m for applied voltages of 150 V, 300 V, 450 V, and 600 V, respectively, with the baseline set at 1.2 S/m. Even at the highest voltages, the noticeable increase in conductivity had an insignificant effect on the electric-field distribution in the current experimental setup. For example, between

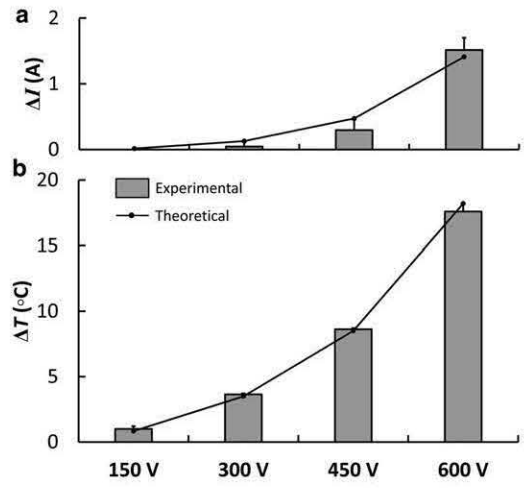

FIGURE 5 Change in current (*a*) and temperature (*b*) delivered through the in vitro tumors during IRE performed at 150 V, 300 V, 450 V, and 600 V. The treatment consisted of 80 100-μs-long pulses delivered at a rate of 1/s. The bars with 1 standard deviation indicate the experimentally measured values. The data points along the line illustrate the results of the numerical model, which was optimized to match the measured changes in current and temperature from onset to offset of pulsing.

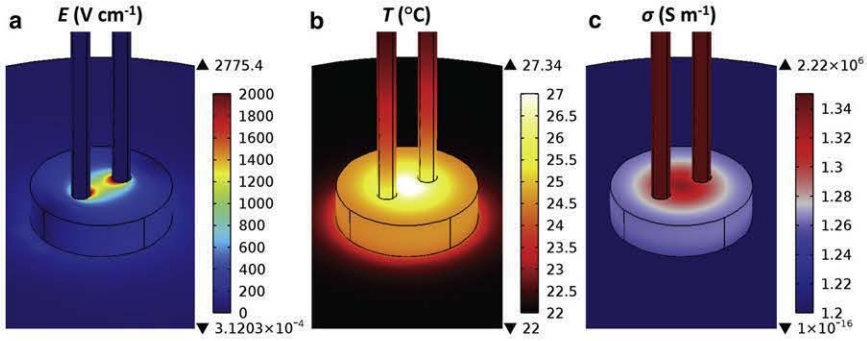

FIGURE 6 Surface plots from the numerical model showing the electric-field distribution (*a*), temperature distribution (*b*), and conductivity distribution (*c*) at the end of an 80-s IRE treatment at 300 V. The upper and lower triangles along the scale bars indicate maximum and minimum values, respectively, present within the entire domain. In the case of (*c*) these values are consistent with those reported in Table 1 for the electrode and plate domains. Regions experiencing values outside the given color range (e.g., electrode and plate conductivity) assume the color associated with the limits of the displayed data.

the onset and offset of pulsing, the area of the top surface of the in vitro tumors exposed to an electric field >500 V/cm changed by 0.01 mm^2, 0.02 mm^2, 0.09 mm^2, and 0.4 mm^2 for applied voltages of 150 V, 300 V, 450 V, and 600 V, respectively. This correlates with a slight change in the dimensions of the 500 V/cm electric-field contour from the onset to offset of pulsing. However, even at 600 V, the height of the area encompassed by the contour (*y*-direction) changed by only 0.08 mm, and the width (*x*-direction) changed by only 0.04 mm. All of these variations are within 1 standard deviation of experimentally measured values (Table 3).

Determination of electric-field threshold for cell death of in vitro tumors

Only applied voltages of 300 V and 450 V were used to determine the electric-field threshold for cell death (Table 3). As mentioned, an applied voltage of 150 V did not produce a complete lesion extending past the lateral surfaces of the electrodes or completely connecting in the center (Fig. 2), which eliminated the possibility of accurate width measurements. At 600 V, void formation at the center of the in vitro tumors, presumably due to collagen denaturation, also eliminated the possibility of accurate measurements. There was a close agreement in the electric-field threshold for cell death as determined by both the 300 V and 450 V treatment groups. In the 300 V group, averaging the electric-field threshold as determined by each separate measurement resulted in a threshold of 497 V/cm. In a similar way, in the 450 V group, the average threshold from each measurement was 490 V/cm. Between the groups, the highest variability was present within thresholds determined from width measurements. This is likely due to the difficulty in measuring lesion width near the electrodes and the steep gradient in electric potential near the lateral electrode surfaces. When width measurements were omitted from the analysis, the electric-field threshold for cell death became 496 V/cm and 500 V/cm for the 300 V and 450 V groups, respectively.

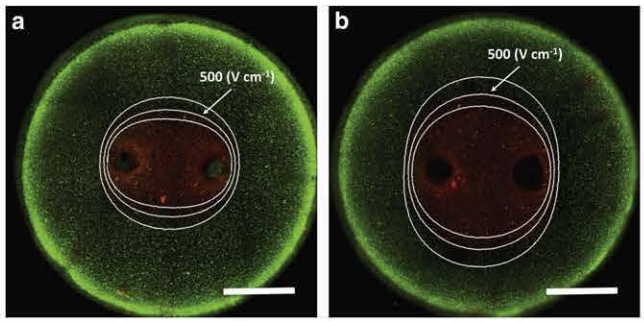

FIGURE 7 Overlay of electric-field contours predicted by the numerical model at the end of 80-s IRE treatments at 300 V (*a*) and 450 V (*b*) with the corresponding live/dead tiled images from Fig. 2. The field contours shown are at 400 V/cm (*inner*), 500 V/cm (*middle*), and 600 V/cm (*outer*). The contour labeled 500 V/cm denotes the threshold for cell death. Scale bars, 2.5 mm.

Overlaying the 500 V/cm contour on the live/dead stained images of the in vitro tumors from each of these groups illustrates the accuracy of the numerical model for determining the electric-field threshold for cell death (Fig. 7). Although no data are present in the literature on the threshold in pancreatic tumors, our result is comparable to that obtained in vivo for brain tissue (23) when a similar pulsing protocol was implemented. Results citing a higher threshold of 637 V/cm in vivo for liver tissue were likely due to a 10-fold reduction in the number of pulses delivered (21), and this effect could be elucidated in future experiments.

Determination of electric-field threshold for cell death in suspension

It is difficult to determine a distinct electric-field threshold for cell death from the viability analysis on cell suspensions. In the past, conservative estimates have been made under the assumption that the threshold in vivo corresponds to the value of the electric field, resulting in <5% viability in suspension (31). Under the same logic, our results suggest that a conservative estimate of the electric-field threshold for cell death in vivo would be ~1500 V/cm (see Fig. S1). In addition, at 500 V/cm there was no corresponding reduction of cell viability in suspension. Similar results have been shown for the onset of reversible electroporation,

which was found to occur at a significantly lower electric-field strength in vivo compared to the same cells in suspension (56).

DISCUSSION

Cancer cells cultured in 3D collagen I hydrogels were shown to respond to IRE pulse delivery comparable to published in vivo results. This included a similar electric-field threshold for cell death (Table 3) (23), sparing of the underlying collagen network (8), and submillimeter resolution at the boundary between treated and untreated regions (Fig. 3) (8,9). Recently, collagen I hydrogels have been used to study reversible electroporation and electrogene transfer (57). In that study, conducted by Haberl and Pavlin, it was found that electrogene transfer had a dependency on plasmid concentration and pulse duration similar to that seen in vivo when performed in a 3D in vitro environment. Further, transfection was more pronounced on the surface of the collagen I hydrogels, due to diffusion limitations through the collagen mesh, which is also a characteristic seen in vivo (58). Outside the field of electroporation, 3D cell culture models have been shown to elicit an in-vivo-like response for other cancer therapies, including chemotherapy (59), radiation therapy (60), and nanoparticle delivery (61). This platform could also be used to optimize therapies that utilize low-intensity alternating electric fields to arrest cell proliferation by disrupting cells during cleavage (62), as opposed to directly inducing cell death through membrane disruption, as shown here.

Compared to conventional in vitro IRE-treatment-planning models, such as cell suspensions and cell-culture monolayers, the 3D in vitro tumor model generated more accurate predictability of IRE outcomes. This is likely due to the ability of the cells cultured in 3D to reproduce the cell-cell/cell-matrix interactions seen in the original tissue that are important for dictating an in-vivo-like morphology. As a result of cell protrusions interacting with the collagen matrix, the cell diameters in the hydrogel are larger than they are in suspension (13.1 μm). This may contribute to the decreased electric-field threshold for cell death, as a larger diameter increases the calculated transmembrane potential (63):

$$\Delta\varphi(\theta) = \frac{3}{2} E\, a \cos(\theta), \tag{6}$$

where a is the radius of the cell and θ is the polar angle measured from the center of the cell with respect to the direction of the electric field. The induced transmembrane potential creates a supraphysiologic electric field in the membrane that is thought to be responsible for permeabilization. For a membrane thickness of 5 nm, an external electric field of 500 V/cm applied across a cell in suspension ($\Delta\varphi_{max}$ = 0.98 V) generates a voltage/distance ratio on the order of ~2 MV/cm within the membrane. In cell monolayers, 2D spatial information and limited cell-cell/cell-matrix interactions can be obtained, but the path taken by electrical current is significantly altered when compared to a 3D environment (a majority of current flows through the culture media over the top of cells that are adhered to a highly insulative surface), which may alter the transmembrane potential and electric-field threshold for cell death. Furthermore, analysis of dead cells is complicated by the fact that they can detach from the culture surface.

Current measurements were unable to detect any dynamic change in bulk electrical conductivity due to electroporation for in vitro tumors consisting of 5×10^6 cells/ml. Specifically, at an applied voltage of 300 V, there was no statistical difference in the change in current between the first and last pulse when comparing the 5×10^6-cells/ml group to the no-cells control group. Therefore, any dynamic changes in bulk-tissue electrical conductivity due to electroporation that have been reported in vivo (64) could be neglected from the numerical model of the in vitro tumor. This greatly reduced the number of parameters contributing to an accurate determination of the electric-field threshold for IRE.

When the cell concentration was increased to 50×10^6 cells/ml, there was a significant decrease in the measured current during treatment at 300 V compared to the no-cells control and 5×10^6-cells/ml groups (data not shown). This is unlike what happens in vivo, and it may be the result of the fact that the cytoplasm has a lower electrical conductivity than the extracellular space (65). Upon electroporation, the release of cytosol into the extracellular space may dominate the bulk electrical properties at this specific cell concentration. At higher cell concentrations in tissue, the bulk electrical properties during electroporation are dominated by the creation of membrane defects, which greatly increase the conductivity and resulting current during treatment. According to the EMT model, a cell concentration on the order of 340×10^6 cells/ml would be required to cut the baseline conductivity of the in vitro tumors in half, from 1.2 S/m to 0.6 S/m, which is more electrically relevant to tissue and corresponds to a volume fraction of 0.4. Due to diffusion limitations through the collagen hydrogel, obtaining such high concentrations while maintaining cell viability is a challenging task. This will be the subject of future work directed toward replicating the dynamic conductivity changes seen in vivo on a 3D in vitro platform.

A current limitation of the relatively high electrical conductivity of the in vitro tumors compared to an in vivo environment is the added heat generated during treatment. As a result, select protocols that do not cause significant thermal damage in vivo may be unsuitable for testing in vitro due to collagen I denaturation. Similar concerns are present when treating cells in suspension. For the range of applicable pulse parameters tested here, thermal changes had a minimal influence on the electric field distribution. This may be attributed to the small size of the in vitro tumor

domain relative to the electrode spacing, which causes the entire tumor to experience both an elevated temperature and conductivity. In the future, the hydrogel volume could be increased to mimic a clinical scenario in which the electrodes are inserted into a targeted tumor and the treatment region varies in all directions. Here, the experimental setup was designed to induce a region of cell death that was symmetric in the z-direction (Fig. 3).

CONCLUSION

Performing IRE on a 3D in vitro tumor platform produced an electric field dependence on cell death characteristic of an in vivo response. Thus, this model is suitable for generating a wide range of data that will be useful in refining treatment-planning algorithms used in clinical IRE procedures. Specifically, studies correlating varying pulse parameters to ablation volume in a variety of cancer cell lines will help identify both protocol-specific and cell-specific parameters to enhance the reliability of predicted outcomes. In addition, there is the possibility of growing patient-specific in vitro tumors from biopsied tissue. Further development of this platform will facilitate the acceptance of IRE as a viable cancer therapy.

SUPPORTING MATERIAL

One figure, supporting references, and a detailed description of IRE pulse delivery and viability analysis for cell suspensions are available at http://www.biophysj.org/biophysj/supplemental/S0006-3495(12)01032-6.

The authors thank Dr. Dieter Saur of the Technische Universität München for generously providing access to the murine PDAC cells.

This work was supported by the National Science Foundation under Awards CAREER CBET-1055913 and CAREER CBET-0955072.

REFERENCES

1. Davalos, R. V., I. L. Mir, and B. Rubinsky. 2005. Tissue ablation with irreversible electroporation. *Ann. Biomed. Eng.* 33:223–231.
2. Garcia, P. A., T. Pancotto, ..., R. V. Davalos. 2011. Non-thermal irreversible electroporation (N-TIRE) and adjuvant fractionated radiotherapeutic multimodal therapy for intracranial malignant glioma in a canine patient. *Technol. Cancer Res. Treat.* 10:73–83.
3. Neal, 2nd, R. E., J. H. Rossmeisl, Jr., ..., R. V. Davalos. 2011. Successful treatment of a large soft tissue sarcoma with irreversible electroporation. *J. Clin. Oncol.* 29:e372–e377.
4. Thomson, K. R., W. Cheung, ..., A. Haydon. 2011. Investigation of the safety of irreversible electroporation in humans. *J. Vasc. Interv. Radiol.* 22:611–621.
5. Bagla, S., and D. Papadouris. 2012. Percutaneous irreversible electroporation of surgically unresectable pancreatic cancer: a case report. *J. Vasc. Interv. Radiol.* 23:142–145.
6. Ball, C., K. R. Thomson, and H. Kavnoudias. 2010. Irreversible electroporation: a new challenge in "out of operating theater" anesthesia. *Anesth. Analg.* 110:1305–1309.
7. Kingham, T. P., A. M. Karkar, ..., Y. Fong. 2012. Ablation of perivascular hepatic malignant tumors with irreversible electroporation. *J. Am. Coll. Surg.* 215:379–387.
8. Onik, G., P. Mikus, and B. Rubinsky. 2007. Irreversible electroporation: implications for prostate ablation. *Technol. Cancer Res. Treat.* 6:295–300.
9. Edd, J. F., L. Horowitz, ..., B. Rubinsky. 2006. In vivo results of a new focal tissue ablation technique: irreversible electroporation. *IEEE Trans. Biomed. Eng.* 53:1409–1415.
10. Onik, G., and B. Rubinsky. 2010. Irreversible electroporation: first patient experience focal therapy of prostate cancer. *In* Irreversible Electroporation. B. Rubinsky, editor. Springer, Berlin/Heidelberg. 235–247.
11. Maor, E., A. Ivorra, and B. Rubinsky. 2009. Non thermal irreversible electroporation: novel technology for vascular smooth muscle cells ablation. *PLoS ONE.* 4:e4757.
12. Li, W., Q. Y. Fan, ..., Z. Li. 2011. The effects of irreversible electroporation (IRE) on nerves. *PLoS ONE.* 6:e18831.
13. Rubinsky, B., G. Onik, and P. Mikus. 2007. Irreversible electroporation: a new ablation modality—clinical implications. *Technol. Cancer Res. Treat.* 6:37–48.
14. Zhang, Y., Y. Guo, ..., A. C. Larson. 2010. MR imaging to assess immediate response to irreversible electroporation for targeted ablation of liver tissues: preclinical feasibility studies in a rodent model. *Radiology.* 256:424–432.
15. Lee, E. W., C. Chen, ..., S. T. Kee. 2010. Advanced hepatic ablation technique for creating complete cell death: irreversible electroporation. *Radiology.* 255:426–433.
16. Deodhar, A., S. Monette, ..., S. B. Solomon. 2011. Percutaneous irreversible electroporation lung ablation: preliminary results in a porcine model. *Cardiovasc. Intervent. Radiol.* 34:1278–1287.
17. Appelbaum, L., E. Ben-David, ..., S. N. Goldberg. 2012. US findings after irreversible electroporation ablation: radiologic-pathologic correlation. *Radiology.* 262:117–125.
18. Ben-David, E., L. Appelbaum, ..., S. N. Goldberg. 2012. Characterization of irreversible electroporation ablation in in vivo porcine liver. *AJR Am. J. Roentgenol.* 198:W62–W68.
19. Bower, M., L. Sherwood, ..., R. Martin. 2011. Irreversible electroporation of the pancreas: definitive local therapy without systemic effects. *J. Surg. Oncol.* 104:22–28.
20. Charpentier, K. P., F. Wolf, ..., D. E. Dupuy. 2010. Irreversible electroporation of the pancreas in swine: a pilot study. *HPB (Oxford).* 12:348–351.
21. Miklavcic, D., D. Semrov, ..., L. M. Mir. 2000. A validated model of in vivo electric field distribution in tissues for electrochemotherapy and for DNA electrotransfer for gene therapy. *Biochim. Biophys. Acta.* 1523:73–83.
22. Sano, M. B., R. E. Neal, ..., R. V. Davalos. 2010. Towards the creation of decellularized organ constructs using irreversible electroporation and active mechanical perfusion. *Biomed. Eng. Online.* 9:83.
23. Garcia, P. A., J. H. Rossmeisl, Jr., ..., R. V. Davalos. 2010. Intracranial nonthermal irreversible electroporation: in vivo analysis. *J. Membr. Biol.* 236:127–136.
24. Neal, 2nd, R. E., R. Singh, ..., R. V. Davalos. 2010. Treatment of breast cancer through the application of irreversible electroporation using a novel minimally invasive single needle electrode. *Breast Cancer Res. Treat.* 123:295–301.
25. Miklavcic, D., D. Sel, ..., L. Mir. 2004. Sequential finite element model of tissue electropermeabilisation. *Conf. Proc. IEEE Eng. Med. Biol. Soc.* 5:3551–3554.
26. Ivorra, A., and B. Rubinsky. 2007. In vivo electrical impedance measurements during and after electroporation of rat liver. *Bioelectrochemistry.* 70:287–295.
27. Pavselj, N., Z. Bregar, ..., D. Miklavcic. 2005. The course of tissue permeabilization studied on a mathematical model of a subcutaneous tumor in small animals. *IEEE Trans. Biomed. Eng.* 52:1373–1381.
28. Garcia, P. A., J. H. Rossmeisl, Jr., ..., R. V. Davalos. 2011. A parametric study delineating irreversible electroporation from thermal damage based on a minimally invasive intracranial procedure. *Biomed. Eng. Online.* 10:34.

29. Neal, 2nd, R. E., P. A. Garcia, ..., R. V. Davalos. 2012. Experimental characterization and numerical modeling of tissue electrical conductivity during pulsed electric fields for irreversible electroporation treatment planning. *IEEE Trans. Biomed. Eng.* 59:1076–1085.
30. Ivorra, A., B. Al-Sakere, ..., L. M. Mir. 2009. In vivo electrical conductivity measurements during and after tumor electroporation: conductivity changes reflect the treatment outcome. *Phys. Med. Biol.* 54:5949–5963.
31. Neal, 2nd, R. E., and R. V. Davalos. 2009. The feasibility of irreversible electroporation for the treatment of breast cancer and other heterogeneous systems. *Ann. Biomed. Eng.* 37:2615–2625.
32. Miller, L., J. Leor, and B. Rubinsky. 2005. Cancer cells ablation with irreversible electroporation. *Technol. Cancer Res. Treat.* 4:699–705.
33. Shafiee, H., P. A. Garcia, and R. V. Davalos. 2009. A preliminary study to delineate irreversible electroporation from thermal damage using the Arrhenius equation. *J. Biomech. Eng.* 131:074509.
34. Ivorra, A., L. M. Mir, and B. Rubinsky. 2010. Electric field redistribution due to conductivity changes during tissue electroporation: experiments with a simple vegetal model. *IFMBE Proc.* 25:59–62.
35. Hjouj, M., and B. Rubinsky. 2010. Magnetic resonance imaging characteristics of nonthermal irreversible electroporation in vegetable tissue. *J. Membr. Biol.* 236:137–146.
36. Yamada, K. M., and E. Cukierman. 2007. Modeling tissue morphogenesis and cancer in 3D. *Cell.* 130:601–610.
37. Kim, J. B. 2005. Three-dimensional tissue culture models in cancer biology. *Semin. Cancer Biol.* 15:365–377.
38. Griffith, L. G., and M. A. Swartz. 2006. Capturing complex 3D tissue physiology in vitro. *Nat. Rev. Mol. Cell Biol.* 7:211–224.
39. Fischbach, C., R. Chen, ..., D. J. Mooney. 2007. Engineering tumors with 3D scaffolds. *Nat. Methods.* 4:855–860.
40. Szot, C. S., C. F. Buchanan, ..., M. N. Rylander. 2011. 3D in vitro bioengineered tumors based on collagen I hydrogels. *Biomaterials.* 32: 7905–7912.
41. Verbridge, S. S., N. W. Choi, ..., C. Fischbach. 2010. Oxygen-controlled three-dimensional cultures to analyze tumor angiogenesis. *Tissue Eng. Part A.* 16:2133–2141.
42. von Burstin, J., S. Eser, ..., D. Saur. 2009. E-cadherin regulates metastasis of pancreatic cancer in vivo and is suppressed by a SNAIL/HDAC1/HDAC2 repressor complex. *Gastroenterology.* 137:361–371, 371, e1–e5.
43. Seidler, B., A. Schmidt, ..., D. Saur. 2008. A Cre-loxP-based mouse model for conditional somatic gene expression and knockdown in vivo by using avian retroviral vectors. *Proc. Natl. Acad. Sci. USA.* 105: 10137–10142.
44. Saur, D., B. Seidler, ..., R. M. Schmid. 2005. CXCR4 expression increases liver and lung metastasis in a mouse model of pancreatic cancer. *Gastroenterology.* 129:1237–1250.
45. Paszek, M. J., N. Zahir, ..., V. M. Weaver. 2005. Tensional homeostasis and the malignant phenotype. *Cancer Cell.* 8:241–254.
46. Al-Sakere, B., F. André, ..., L. M. Mir. 2007. Tumor ablation with irreversible electroporation. *PLoS ONE.* 2:e1135.
47. Pavselj, N., and D. Miklavcic. 2011. Resistive heating and electropermeabilization of skin tissue during in vivo electroporation: a coupled nonlinear finite element model. *Int. J. Heat Mass Transf.* 54:2294–2302.
48. Edd, J. F., and R. V. Davalos. 2007. Mathematical modeling of irreversible electroporation for treatment planning. *Technol. Cancer Res. Treat.* 6:275–286.
49. Pavlin, M., T. Slivnik, and D. Miklavcic. 2002. Effective conductivity of cell suspensions. *IEEE Trans. Biomed. Eng.* 49:77–80.
50. Polk, C., and E. Postow. 1996. Handbook of Biological Effects of Electromagnetic Fields. CRC Press, Boca Raton, FL.
51. Schwan, H. P., and K. R. Foster. 1980. Rf-field interactions with biological systems: electrical properties and biophysical mechanisms. *Proc. IEEE.* 68:104–113.
52. Arena, C. B., M. B. Sano, ..., R. V. Davalos. 2011. High-frequency irreversible electroporation (H-FIRE) for non-thermal ablation without muscle contraction. *Biomed. Eng. Online.* 10:102.
53. Kanthou, C., S. Kranjc, ..., M. Cemazar. 2006. The endothelial cytoskeleton as a target of electroporation-based therapies. *Mol. Cancer Ther.* 5:3145–3152.
54. Chapman, A. J. 1987. Fundamentals of Heat Transfer. Macmillan, London.
55. Bozec, L., and M. Odlyha. 2011. Thermal denaturation studies of collagen by microthermal analysis and atomic force microscopy. *Biophys. J.* 101:228–236.
56. Belehradek, Jr., J., S. Orlowski, ..., L. M. Mir. 1994. Electropermeabilization of cells in tissues assessed by the qualitative and quantitative electroloading of bleomycin. *Biochim. Biophys. Acta.* 1190:155–163.
57. Haberl, S., and M. Pavlin. 2010. Use of collagen gel as a three-dimensional in vitro model to study electropermeabilization and gene electrotransfer. *J. Membr. Biol.* 236:87–95.
58. Henshaw, J. W., and F. Yuan. 2008. Field distribution and DNA transport in solid tumors during electric field-mediated gene delivery. *J. Pharm. Sci.* 97:691–711.
59. dit Faute, M. A., L. Laurent, ..., H. Bobichon. 2002. Distinctive alterations of invasiveness, drug resistance and cell-cell organization in 3D-cultures of MCF-7, a human breast cancer cell line, and its multidrug resistant variant. *Clin. Exp. Metastasis.* 19:161–168.
60. St Croix, B., V. A. Florenes, ..., R. S. Kerbel. 1996. Impact of the cyclin-dependent kinase inhibitor p27Kip1 on resistance of tumor cells to anticancer agents. *Nat. Med.* 2:1204–1210.
61. Lee, J., G. D. Lilly, ..., N. A. Kotov. 2009. In vitro toxicity testing of nanoparticles in 3D cell culture. *Small.* 5:1213–1221.
62. Kirson, E. D., V. Dbalý, ..., Y. Palti. 2007. Alternating electric fields arrest cell proliferation in animal tumor models and human brain tumors. *Proc. Natl. Acad. Sci. USA.* 104:10152–10157.
63. Schwan, H. P. 1957. Electrical properties of tissue and cell suspensions. *Adv. Biol. Med. Phys.* 5:147–209.
64. Davalos, R. V., D. M. Otten, ..., B. Rubinsky. 2004. Electrical impedance tomography for imaging tissue electroporation. *IEEE Trans. Biomed. Eng.* 51:761–767.
65. Mezeme, M. E., G. Pucihar, ..., D. Miklavcic. 2012. A numerical analysis of multicellular environment for modeling tissue electroporation. *Appl. Phys. Lett.* 100:143701–143705.
66. Reference deleted in proof.
67. Chiu, J., and P. G. Fair. 1979. Determination of thermal conductivity by differential scanning calorimetry. *Thermochim. Acta.* 34:267–273.